Magnetic Resonance in Medicine

Feasibility of dynamic T_2*-based oxygen-enhanced lung MRI at 3T

Mina Kim[1] | **Josephine H. Naish**[2,3] | **Sarah H. Needleman**[1] | **Marta Tibiletti**[2] | **Yohn Taylor**[1] | **James P. B. O'Connor**[4,5] | **Geoff J. M. Parker**[1,2]

[1]Department of Medical Physics and Biomedical Engineering, Centre for Medical Image Computing (CMIC), University College London, London, UK

[2]Bioxydyn Limited, Manchester, UK

[3]BHF Manchester Centre for Heart and Lung Magnetic Resonance Research (MCMR), Manchester University NHS Foundation Trust, Manchester, UK

[4]Division of Cancer Sciences, University of Manchester, Manchester, UK

[5]Division of Radiotherapy and Imaging, Institute of Cancer Research, London, UK

Correspondence
Geoff J. M. Parker, Centre for Medical Image Computing (CMIC), University College London, London, UK.
Email: geoff.parker@ucl.ac.uk

Abstract

Purpose: To demonstrate proof-of-concept of a T_2*-sensitized oxygen-enhanced MRI (OE-MRI) method at 3T by assessing signal characteristics, repeatability, and reproducibility of dynamic lung OE-MRI metrics in healthy volunteers.

Methods: We performed sequence-specific simulations for protocol optimisation and acquired free-breathing OE-MRI data from 16 healthy subjects using a dual-echo RF-spoiled gradient echo approach at 3T across two institutions. Non-linear registration and tissue density correction were applied. Derived metrics included percent signal enhancement (PSE), ΔR_2* and wash-in time normalized for breathing rate (τ-nBR). Inter-scanner reproducibility and intra-scanner repeatability were evaluated using intra-class correlation coefficient (ICC), repeatability coefficient, reproducibility coefficient, and Bland–Altman analysis.

Results: Simulations and experimental data show negative contrast upon oxygen inhalation, due to substantial dominance of ΔR_2* at TE > 0.2 ms. Density correction improved signal fluctuations. Density-corrected mean PSE values, aligned with simulations, display TE-dependence, and an anterior-to-posterior PSE reduction trend at TE_1. ΔR_2* maps exhibit spatial heterogeneity in oxygen delivery, featuring anterior-to-posterior R_2* increase. Mean T_2* values across 32 scans were 0.68 and 0.62 ms for pre- and post-O_2 inhalation, respectively. Excellent or good agreement emerged from all intra-, inter-scanner and inter-rater variability tests for PSE and ΔR_2*. However, ICC values for τ-nBR demonstrated limited agreement between repeated measures.

Conclusion: Our results demonstrate the feasibility of a T_2*-weighted method utilizing a dual-echo RF-spoiled gradient echo approach, simultaneously capturing PSE, ΔR_2* changes, and oxygen wash-in during free-breathing. The excellent or good repeatability and reproducibility on intra- and inter-scanner PSE and ΔR_2* suggest potential utility in multi-center clinical applications.

KEYWORDS
3T, dynamic, free-breathing, lung, OE-MRI, oxygen-enhanced MRI, repeatability, reproducibility

1 | INTRODUCTION

Oxygen-enhanced MRI (OE-MRI) is a method that has been demonstrated for imaging lung function.[1,2] To date, the majority of OE-MRI studies have made use of T_1-weighted acquisitions, which enable regional investigation of oxygen delivery to the tissues and blood pool via ventilation and gas exchange across the alveolar epithelium into the bloodstream, since a change in T_1 occurs due to the paramagnetic nature of oxygen dissolved in the parenchyma. During the past two decades, investigators have shown promising OE-MRI results for evaluating abnormal lung function in patients with chronic lung disease including interstitial pneumonia, pulmonary emphysema, cystic fibrosis, pulmonary thromboembolism, chronic obstructive pulmonary disease (COPD), lung cancer, and asthma.[3–9]

To date, most OE-MRI studies in lungs have been performed at field strengths of 1.5T or lower,[10] while there is a scarcity of literature on OE-MRI methods at 3T. Previous studies at 3T used T_1-weighted single-slice non-selective inversion-recovery half-Fourier acquisition single-shot turbo spin echo (HASTE),[11] 3D radial UTE pulse sequence with HASTE acquisition,[12] and 3D T_1-weighted fast-field echo (FFE).[13] While all these methods used separate free-breathing acquisitions at 21% and 100% O_2, methodologies for free-breathing lung OE-MRI over entire time course enabling dynamic parametrisation have not been established at 3T.

There are inherent difficulties in conducting lung MRI at 3T. The magnetic susceptibility differences at the numerous air–tissue interfaces within the lung are greater than at lower field strengths and significantly shorten T_2^* in the parenchyma, thereby reducing the signal available for gradient echo-based methods. Additionally, T_1 relaxivity of oxygen decreases with increased field strength,[14] further diminishing the sensitivity of the commonly-used ΔR_1-based OE-MRI methods. Moreover, when employing gradient echo-based methods, the competing ΔR_2^* effect becomes substantial and dominates over the ΔR_1 effect at 3T, even at short TE.[15] Nevertheless, spoiled gradient echo pulse sequences are the most widely used methods for dynamic MRI data collection, enabling rapid acquisition of images with good spatial coverage and resolution. Although spin echo-based and ultrafast echo-based methods are not compromised by T_2^* effects, they may be limited to T_1-sensitized "static" (e.g., breath-hold or gated) OE-MRI due to relatively low temporal resolution.

Given the increasing clinical availability of 3T MRI, the above technical challenges underscore the necessity for novel methodological advancements, aiming to facilitate the widespread adoption of dynamic OE-MRI at 3T. We hypothesized that T_2^*-sensitized dynamic OE-MRI, characterized by a dual-echo acquisition, can enhance the sensitivity of lung signal detection and this work is motivated by a need to evaluate the performance of our proposed method. Furthermore, in order for OE-MRI to find application in clinical research and, ultimately, clinical practice, it is important to harmonize protocols across centers and vendors. Additionally, any derived biomarkers must exhibit satisfactory levels of repeatability and reproducibility.[16]

The primary objective of the present study was to demonstrate proof-of-concept of the T_2^*-sensitized method and an initial assessment of its robustness. Specifically, we aimed (1) to use simulations to characterize the OE-MRI signal across a range of achievable sequence parameters at 3T; (2) to evaluate the feasibility of the T_2^*-sensitized OE-MRI method at 3T in healthy volunteers; and (3) to assess the repeatability and reproducibility of the dynamic OE-MRI metrics in healthy volunteers across two sites and two vendors.

2 | METHODS

For dynamic multi-slice OE-MRI acquisition, we implemented a dual-echo RF-spoiled gradient echo sequence to enable estimation of T_2^*. We aimed to obtain images with a high temporal resolution to minimize motion artifact during free-breathing while maximizing lung coverage and enabling reasonable spatial resolution. We determined that $TR = 16\,ms$ and matrix size $= 96 \times 96$, would enable dynamic temporal resolution $<2\,s$ and acquisition of six slices. Both TEs for the dual-echo acquisition should be as short as possible to avoid losing signal due to low T_2^*, and flip angle (FA) should be chosen to maximize signal difference between normoxia and hyperoxia. The human data experimental workflow is outlined in Figure S1 (Supporting Information).

2.1 | Simulations

We simulated the signal behavior of the dual-echo RF-spoiled gradient echo sequence at our chosen TR (16 ms) over a range of FA and TE values to match the experimental sequence and protocol, described as follows.[17] First, the expected signal difference between air breathing and 100% oxygen breathing (ΔS) and percent signal enhancement (PSE; $100\% \times \Delta S/S(air)$) in the lung was simulated as a function of FA up to 30° and TE up to 3 ms using the following parameters: T_1 (air) $= 1281\,ms$,[18] T_1 (100% O_2) $= 1102\,ms$,[18] T_2^* (air) $= 0.68\,ms$, and T_2^* (100% O_2) $= 0.62\,ms$. Given the absence of previously

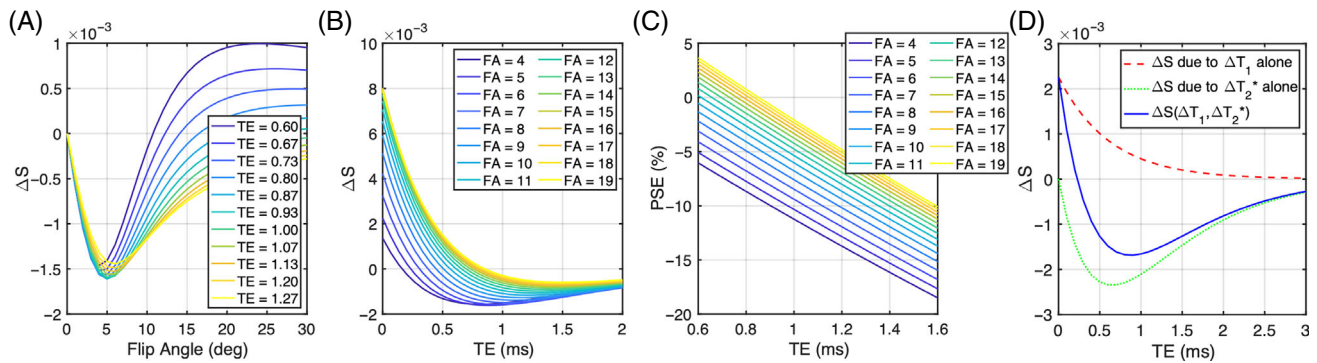Mina Kim and Josephine H. Naish contributed equally to this study.

FIGURE 1 (A) The predicted OE signal change ΔS plotted as a function of flip angle at multiple TE, with $TR = 16$ ms. (B) The predicted signal change ΔS plotted as a function of TE with multiple flip angle, with $TR = 16$ ms. (C) PSE plotted as a function of TE at multiple flip angles, with $TR = 16$ ms. (D) The expected OE signal change for the T_1-weighted RF spoiled gradient echo acquisition at 3T due to ΔT_1 alone (red dashed line), ΔT_2^* alone (green dotted line), and both (blue solid line), assuming literature-reported values for T_1 and measured T_2^* in the lungs at 21% oxygen and 100% oxygen, flip angle = 5°, and $TR = 16$ ms.

reported lung hyperoxic T_2^* values in the literature, we computed T_2^* values for all subjects in our study, then averaged those values for use in the simulations (Table S1). Then, the expected ΔS values were simulated as a function of TE using FA of 5°, which was shown to maximize the absolute signal difference between the 21% and 100% oxygen images. Simulations were performed in MATLAB R2022b (MathWorks, Natick, MA).

2.2 | Participants

Following local research ethics committee approval (Ref: 18837/001) and written informed consent, we recruited 16 healthy volunteers with no previous record of lung diseases. Of these, eight subjects (three males, age range = 26–54 y, median = 39.5 y) underwent lung MRI on a 3T scanner from two vendors in different cities (Philips Ingenia in London, and Siemens MAGNETOM Vida in Manchester, UK) at a 4-wk interval. Eight separate subjects (four males, age range = 23–51 y, median = 27) were scanned twice to assess scan-rescan repeatability at a 4- to 6-wk interval using the Philips scanner. The inclusion criteria for participants specified healthy adult volunteers aged 18–80 y, who self-declared absence of current or previous lung diseases and exhibited no MRI contraindications.

2.3 | MRI acquisition

Where possible, protocols for the two different scanner manufacturers utilized identical acquisition parameters for a 2D interleaved multi-slices dual-echo RF-spoiled gradient echo sequence, while some options required manufacturer-specific parameters. Site-independent

parameters included: six coronal slices of 10 mm thickness with 4 mm gap with phase-encoding right/left; in-plane resolution 4.69×4.69 mm^2; FOV covering entire lungs in all 16 volunteers (except for the inter-slice gaps in the anterior/posterior direction); $TR = 16$ ms; matrix size $= 96 \times 96$; and dynamic temporal resolution $= 1.54$ s. Selection of FA (5°) was based on our simulations (Figure 1). The shortest TE values available for the chosen acquisition were selected for each scanner (L, Philips in London; M, Siemens in Manchester): $TE_{1L} = 0.71$ ms, $TE_{2L} = 1.2$ ms; $TE_{1M} = 0.81$ ms, $TE_{2M} = 1.51$ ms. Scan parameters for each vendor are listed in Table 1.

Subjects were fitted with a disposable/MRI-compatible non-rebreathing mask (Intersurgical, Berkshire, UK) to allow for medical air and 100% oxygen delivery while lying supine in the scanner. Piped gases were delivered to the subject at 15 L/min using a standard low flow oxygen blender (Inspiration Healthcare, Leicestershire, UK). The initial 60 dynamic acquisitions were obtained while breathing medical air. The gas supply was then switched to 100% O_2 for the following 150 dynamic acquisitions, after which the supply was returned to medical air for further 130 acquisitions. Images were acquired during uncontrolled free-breathing to minimize participant burden and avoid interrupting gas delivery. Total scanning time for the dynamic series was approximately 9 min.

2.4 | Data analysis

For motion correction, non-linear image registration was performed on the dynamic time series data using Advanced Normalization Tools (ANTs).[19,20] Subsequently, the lung parenchyma, excluding central major vasculature, was manually segmented from registered images. For an initial exploration of the data, first, image

TABLE 1 Scan parameters.

	Scanner in London	Scanner in Manchester
Manufacturer	Philips	Siemens
Model	Ingenia	MAGNETOM Vida
Field strength (T)	3.0	2.9
RF coil used	32-channel torso coil in combination with the posterior coil	18-channel body coil in combination with the 32-channel spine coil
Max. gradient strength (mT/m)	45	45
Max. slew rate (T/m/s)	200	200
TR (ms)	16	16
Echoes	Full	Half
Minimum achievable TE_1 (ms)	0.71	0.81
Minimum achievable TE_2 (ms)	1.2	1.51
FOV (mm × mm)	450 × 450	450 × 450
No. of slices	6	6
Slice thickness (mm)	10	10
Gap (mm)	4	4
Acquired matrix	96 × 96	96 × 96
Orientation	Coronal	Coronal
Pixel size (mm × mm)	4.7 × 4.7	4.7 × 4.7
Flip angle (°)	5	5
Bandwidth (Hz/Px)	4488	2000
Parallel imaging	N	N
NSA	1	1
Time resolution (s)	1.54	1.54
Number of dynamics	340	340

registration and density correction were performed as described below. Secondly, averaged hyperoxia images (61st to 210th) were subtracted from averaged normoxia images (10th to 60th). Last, mean PSE maps was calculated from the subtracted images normalized to the averaged normoxia images.

For our main data analysis, the dynamic series were fitted using exponential functions to characterize oxygen wash-in (encompassing the downslope between the plateau regions of the curve) and wash-out (the upslope and return to baseline). The baseline for the exponential fit was defined as the averaged signal intensity across all normoxia time points before O_2 inhalation as described in Eq. 1. The curve was fitted with the two functional forms described in Eq. 2 for the downslope and Eq. 3 for the upslope,

$$A_1(\mathbf{x}) = \frac{\sum S(t, \mathbf{x})}{\text{tp1}}, 1 \leq t \leq \text{tp1} \quad (1)$$

$$S(t, \mathbf{x}) = [A_1(\mathbf{x}) - A_2(\mathbf{x})] \cdot e^{-t/\tau(\mathbf{x})} + A_2(\mathbf{x}), \text{tp1} + 1 \leq t \leq \text{tp2} \quad (2)$$

$$S(t, \mathbf{x}) = [A_1(\mathbf{x}) - A_2(\mathbf{x})] \cdot \left(1 - e^{-t/\tau(\mathbf{x})}\right) + A_2(\mathbf{x}), \text{tp2} + 1 \leq t \quad (3)$$

where $A_1(\mathbf{x})$ and $A_2(\mathbf{x})$ are the baseline and fitted negative maximum hyperoxia intensity (or plateau value) at position $\mathbf{x}$, respectively, and τ, tp1, and tp2 are the fitted wash-in time and the provided gas switching time points (i.e., tp1, air to O_2; tp2, O_2 to air). Maximum PSE maps were produced by the subtraction of the baseline from the negative maximum hyperoxia value ($A_1 - A_2$), normalized to the baseline A_1. We additionally defined a breathing rate-normalized wash-in time, τ-nBR as the product of τ and the average breathing rate over the dynamic series.

As differences in lung tissue density can influence the measured signal enhancement between normoxia and hyperoxia, time-varying PSE maps were calculated twice, with and without a voxel-wise tissue density correction.

Uncorrected PSE values were calculated by the subtraction of normoxia signal (S_{21}) from hyperoxia signal (S_{100}), normalized to S_{21} as.

$$PSE\_u(t, \mathbf{x}) = \frac{S_{100}(t, \mathbf{x}) - S_{21}(\mathbf{x})}{S_{21}(\mathbf{x})} \times 100\%. \qquad (4)$$

Tissue density variation was corrected using the adapted sponge model.[21–24] The whole-lung fractional volume change V was calculated at each time point by averaging the Jacobian determinant from the registration over all voxels in the lung mask across all slices. The Jacobian determinant was only used to obtain an estimate of lung volume change, with density correction based on the signal intensity variation associated with the lung volume change as described further below. The respiratory index α_{local} was estimated voxel-wise (locally at the position $\mathbf{x}$) by linear regression estimation of the observed signal intensity S as a function of V as

$$\alpha_{local}(t, \mathbf{x}) = -\frac{\partial(\log(S(t, \mathbf{x})))}{\partial(\log(V(t, \mathbf{x})))}. \qquad (5)$$

Then, the α_{local} values were applied as a voxel-wise density correction as

$$S_C(t, \mathbf{x}) = S(t, \mathbf{x})V(t, \mathbf{x})^{-\alpha_{local}(t, \mathbf{x})} \qquad (6)$$

where $S_C(t, \mathbf{x})$ represent the corrected $S(t, \mathbf{x})$. Corrected PSE values were quantified as

$$PSE\_c(t, \mathbf{x}) = \frac{S_{100c}(t, \mathbf{x}) - S_{21c}}{S_{21c}} \times 100\% \qquad (7)$$

where $S_{100c}(t, \mathbf{x})$ and $S_{21c}(t, \mathbf{x})$ represent the corrected $S_{100}(t, \mathbf{x})$ and $S_{21}(t, \mathbf{x})$, respectively. To compare pre- and post-density correction, we calculated median PSE values within masks at each TE twice, either across all six slices or the two most posterior slices, excluding anterior slices with poor SNR. The median PSE value for each slice was then averaged across all subjects. For intra-scanner repeatability, median PSE values were averaged over all six slices at each TE.

The R_2^* of each voxel was quantified analytically from the magnitude-reconstructed signal from the masked lung images acquired at TE_1 and TE_2 after tissue density correction as described in Eqs. 5 and 6. ΔR_2^* maps were calculated by the subtraction of mean normoxia R_2^* maps across multiple time points (30th to 60th time series acquisitions) from mean hyperoxia R_2^* maps across multiple time points (120th to 180th). Median ΔR_2^* values were averaged over the two most posterior slices for multi-site comparison between Manchester and London, and six slices for scan-rescan comparison in London.

Data were analyzed by an experienced (>10 years) MRI physicist using a computational pipeline written in MATLAB R2022b (MathWorks, Natick, MA), taking ~60 min per subject visit, primarily due to motion correction.

2.5 | Statistical analysis

Normality was assessed for all metrics using the Shapiro–Wilk test. For non-normally distributed metrics, we log-transformed the data before statistical analyzes (Figure S1). We used Bland–Altman plots with 95% limits of agreement (LOA) and derived the repeatability coefficient (RC), reproducibility coefficient (RDC), and intraclass correlation coefficient (ICC) to evaluate the agreement of repeated measures, as recommended in the QIBA guidelines.[25] For the log-transformed metric, we calculated the asymmetric cut-points for RC and RDC through back-transformation,[26] and ICC values were computed as described in Pleil et al.[27] An inter-rater ICC analysis was conducted on London data from eight volunteers at the initial time point, using additional lung masks outlined by a second rater. The agreement levels were: excellent for ICC > 0.74, good for ICC 0.6–0.74, fair for ICC 0.4–0.59, and poor for ICC < 0.4.[28] Coefficient of variation (CV) was calculated across all subjects at each TE. All statistical analyzes were performed using SPSS v28.0 (SPSS Inc, Chicago, IL).

3 | RESULTS

3.1 | The effect of oxygen on signal intensity–simulations

Simulations show that ΔT_2^*-induced negative enhancement (ΔS) for our chosen TR = 16 ms is maximum at FA ~5°, independent of the choice of TE (Figure 1A). The amplitude of the TE dependence of ΔS reduces with smaller FA (Figure 1B), with negative-going signal change occurring at shorter TE. The magnitude of negative PSE increases with lower FA and longer TE, while PSE values are closer to 0 at shorter TE and high FA (Figure 1C). We also observed that ΔT_2^* dominates the signal change and produces negative contrast at TE > 0.2 ms for FA = 5° (Figure 1D). The expected signal change at TE_{1L} (0.71 ms) is about 55% more sensitive to changes in ΔT_1 and about 21% more sensitive to changes in ΔT_2^* than at TE_{2L} (1.2 ms) (Figure 1D).

3.2 | The effect of oxygen on signal intensity–experimental

Typical location of the acquired images is shown in Figure 2A. PSE maps at both TEs demonstrate uniform
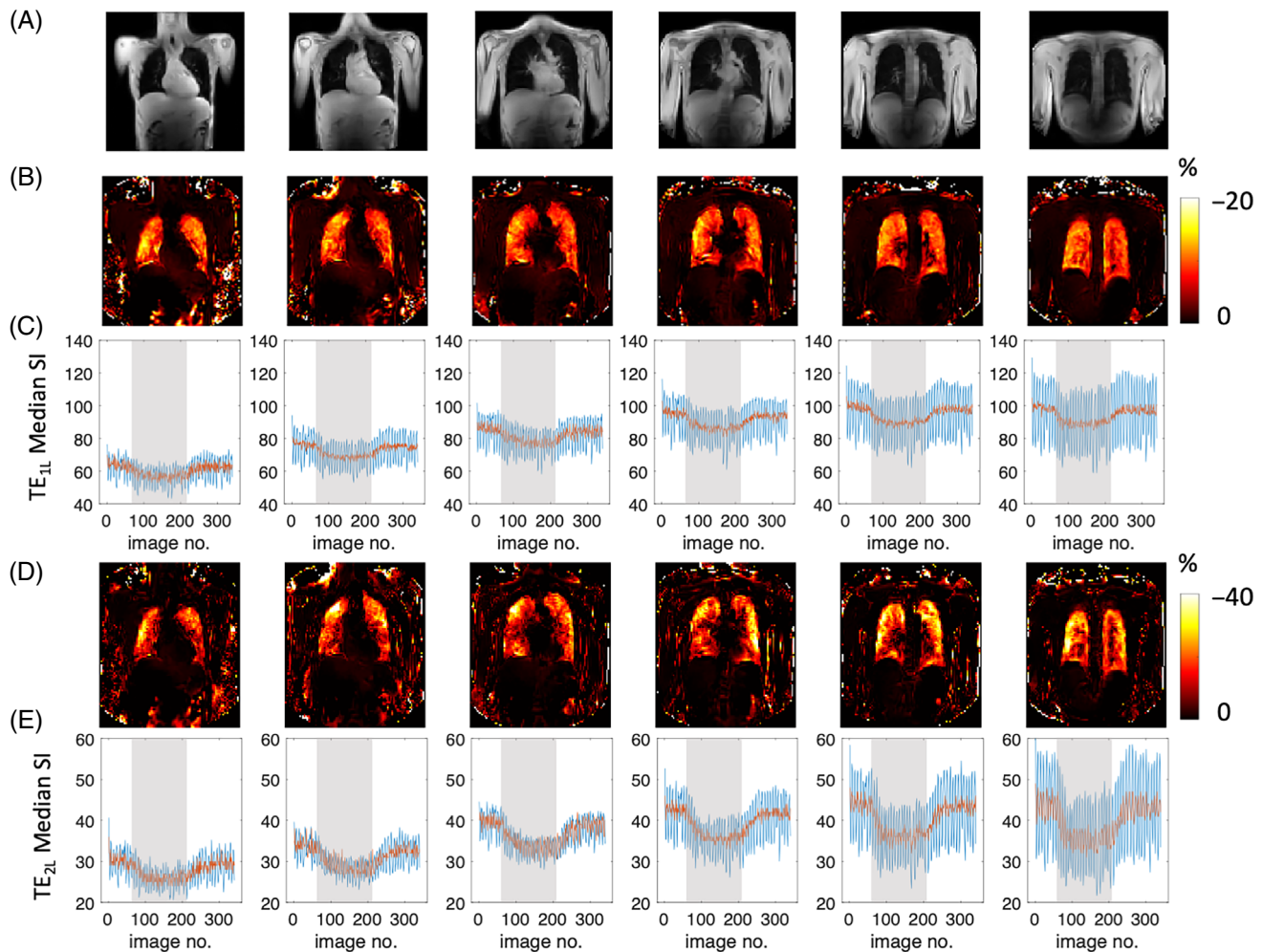
FIGURE 2 (A) The typical location of the six slices from anterior to posterior. Example subject data show unmasked percentage signal change maps obtained with (B) TE_{1L} (0.71 ms) and (D) TE_{2L} (1.2 ms), and (C, E) the corresponding time course curves of the median signal intensity from masked, registered lung for each slice. Blue lines show uncorrected signal; red line shows signal after density correction.

PSE across the parenchyma (Figure 2B,D). As expected, due to the dominant effect of T_2^* changes, time course plots of mean PSE from masked lungs exhibit negative contrast induced by 100% O_2 inhalation (Figure 2C,E), in agreement with the simulated results (Figure 1D). The median signal intensity is higher in posterior slices due to greater proton density, associated with the subjects' supine position (Figures 2C,E and S2).

3.3 | The effect of density correction

The time course plots (Figure 2C,E) post-density correction (red solid line) show smaller magnitude signal fluctuation than pre-density correction (blue solid line) due to the reduced impact of respiratory motion-induced signal changes. Example signal time courses with their downslope and upslope fits (Eqs. 2 and 3) also show improvement in time course wash-in fitting with tissue density correction (Figure S3).

Table 2 summarizes the mean PSE and CV before and after applying density correction for the evaluation of inter-scanner TE-dependence. Across eight healthy volunteers, the magnitudes of all negative PSE values were reduced by applying tissue density correction. Moreover, this correction enhanced the linearity of the reduction in negative PSE magnitudes. In addition, CV of mean PSE was also decreased for all except TE_{1M} PSE (mean PSE values over two posterior slices) or TE_{2M} PSE (mean PSE values over all six slices). All repeatability metrics were improved by the density correction step (Figure S4) as also described in the Section 3.7.

3.4 | TE dependence

While the mean signal intensity is higher at TE_{1L} than for TE_{2L} (Figure 2C,E), PSE is greater at TE_{2L} than at TE_{1L} (Figure 2B,D), again in agreement with our simulations (Figure 1B,C). The TE dependence of PSE expected

TABLE 2 Inter-scanner TE-dependence assessment of uncorrected and corrected mean ($\pm$SD) PSE measurements from eight traveling healthy volunteers in four different TEs (TE_{1L} and TE_{2L} in London; TE_{1M} and TE_{2M} in Manchester).

		TE (ms)	Averaged over two posterior slices		Averaged over all six slices	
			Mean PSE (%) $\pm$ SD (%)	CV (%)	Mean PSE (%) $\pm$ SD (%)	CV (%)
Uncorrected PSE mapping (Eq. 4)	TE_{1L} PSE	0.71	-9.61 ± 4.24	44.13	-9.40 ± 2.28	24.28
	TE_{1M} PSE	0.81	-8.61 ± 1.97	22.84	-9.68 ± 1.69	17.41
	TE_{2L} PSE	1.20	-14.87 ± 4.51	30.35	-14.98 ± 3.31	22.12
	TE_{2M} PSE	1.51	-14.01 ± 2.77	19.80	-11.43 ± 1.53	13.40
Corrected PSE mapping (Eq. 7)	TE_{1L} PSE	0.71	-6.55 ± 1.92	29.32	-6.81 ± 1.47	21.62
	TE_{1M} PSE	0.81	-8.06 ± 1.84	22.85	-9.46 ± 1.82	19.28
	TE_{2L} PSE	1.20	-12.20 ± 2.75	22.56	-11.92 ± 1.78	14.98
	TE_{2M} PSE	1.51	-13.37 ± 2.46	18.39	-11.14 ± 1.73	15.55

Note: The mean PSE and CV were calculated across all subjects at each TE based on the measurement from the two most posterior slices and all six slices.

from simulations (Figure 1C) is also observed in the density-corrected PSE values from four separate TEs at two sites (Table 2).

3.5 | ΔR_2^* quantification

Figure 3 shows examples of plateau ΔR_2^* maps across six slices from anterior to posterior, the corresponding time course plots of the median R_2^* from the maps of masked lungs for each slice. Median ΔR_2^* maps illustrate clear O_2 delivery in the entire lung (Figure 3A,C,E), with a spatial distribution that is heterogeneous compared to the patterns observed in the PSE maps (Figure 2).

Median R_2^* time course plots show R_2^* is largely unaffected by density correction (because the calculation of R_2^* normalizes for density) except for the last posterior slice. We observed that the discrepancy between tissue density corrected (red) and uncorrected (blue) ΔR_2^* plots (Figure 3B) is a common occurrence among volunteers with smaller lung volumes. In such cases, the final posterior slice is aligned with the rear of the lungs, adjacent to the ribcage (Figure 3A) and appears to be influenced by the partial volume effects.

A trend of ΔR_2^* increase from anterior to posterior slices is observed (Figure 4C), and the mean T_2^* values of 16 healthy volunteers from the two posterior slices were 0.68 ± 0.05 ms (T_2^* for 21% O_2) and 0.62 ± 0.05 ms (T_2^* for 100% O_2), while mean ΔR_2^* was 0.14 ± 0.03 ms^{-1} (Table 3).

3.6 | Signal variation with slice position in the lung

The PSE of TE_{1L} gradually decreases from anterior to posterior slices across all subjects (Figure 4A), whereas the

PSE of TE_{2L} do not noticeably change (Figure 4B). ΔR_2^* shows a gradual increase from anterior to posterior.

3.7 | Repeatability and reproducibility

All metrics were normally distributed except a subset of τ-nBR (Table S2).

Example intra-scanner PSE maps show relatively homogeneous enhancement at both TEs (Figure 5A,B). The mean PSE values from eight healthy volunteers varied little between the repeat scans.

The plateau $\triangle R_2^*$ maps from the same data set show relatively heterogeneous $\triangle R_2^*$ distribution, wherein certain structures, particularly areas of major vasculature, do not appear to respond to 100% O_2 inhalation (Figure 5C). This is expected as the R_2^* change is mainly due to gaseous oxygen in the alveoli but not dissolved oxygen as previously reported.[15]

The Bland–Altman plot analyzes of the repeated measurements of PSE and $\triangle R_2^*$ indicate little and insignificant bias between two intra-scanner measurements in London, respectively, as shown by the 95% LOA (Figure 5D–F). The ICC and RC measurements of PSE at TE_{1L} and TE_{2L}, and intra-scanner $\triangle R_2^*$ show excellent intra-scanner repeatability (Table 3).

The PSE maps from inter-scanner traveling volunteers' scans show similar spatial distribution of enhancement at TE_1. However, the PSE observed at TE_2 from the Manchester site exhibits more pronounced noise, which could be attributed to the signal approaching the noise floor at the longer TE (Figure 6A). Plots of the combined PSE values at four separate TEs from the two MRI systems display the expected TE dependence of the signal (Figure 6B, Table 2), similar to simulation (Figure 1C).
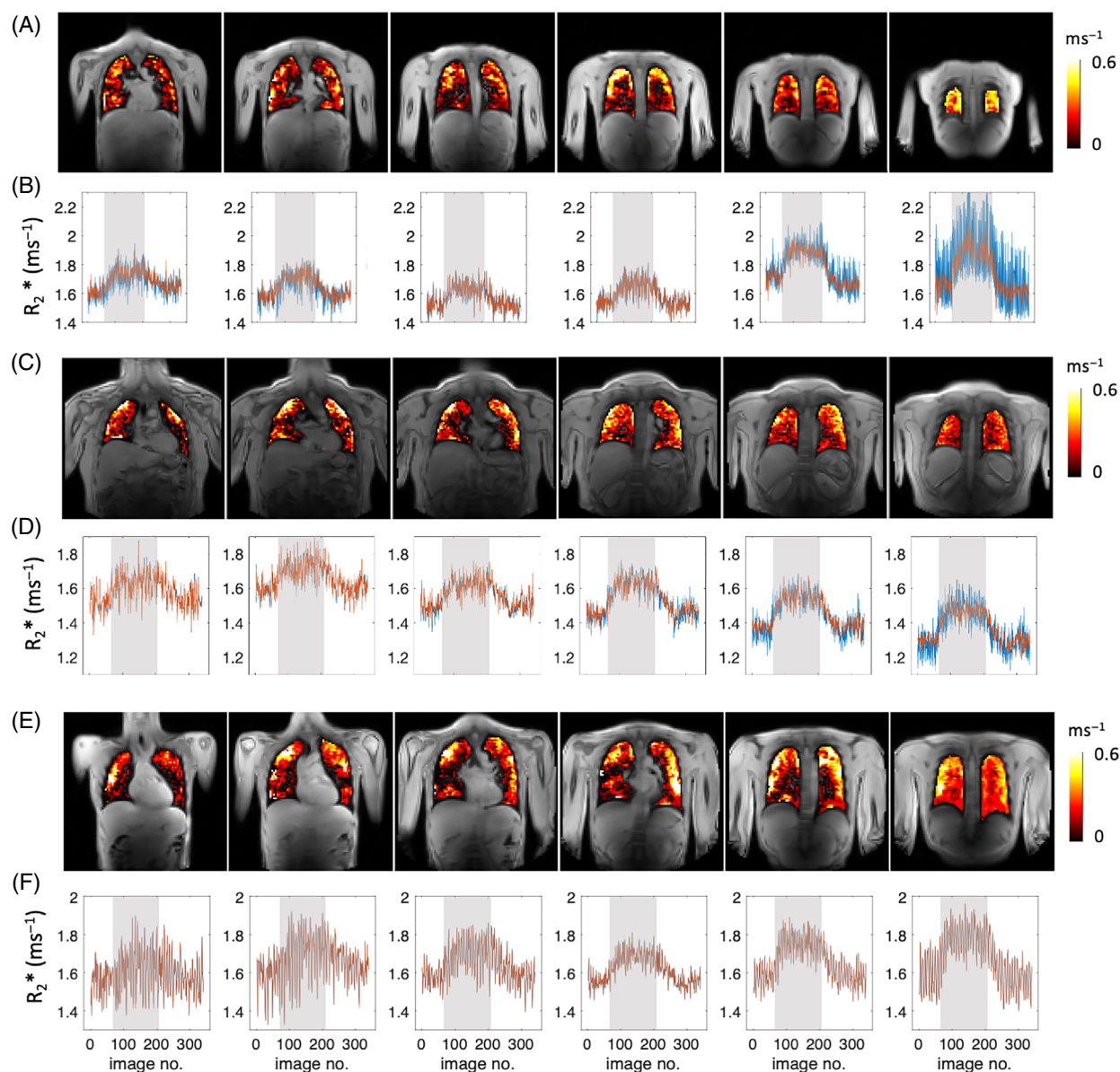
FIGURE 3 Examples of three subjects: (A, C, E) the plateau ΔR_2^* maps of masked lung, six slices from anterior to posterior and (B, D, F) the corresponding time course curves of median R_2^* from masked lung along for each slice. Increase of R_2^* due to 100% O_2 inhalation is visible in all slices but clearer in posterior slices.
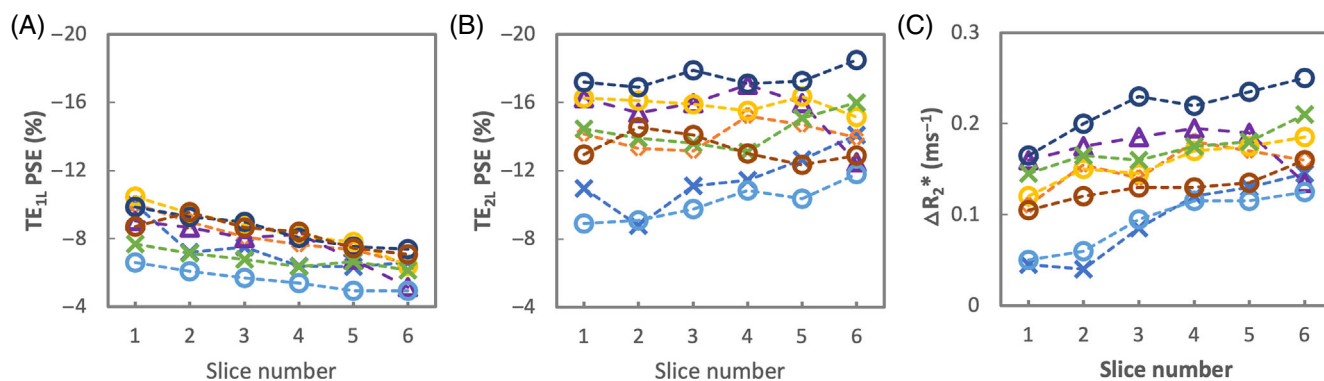

FIGURE 4 The PSE from masked, registered, tissue density corrected lung for each slice of eight individual subjects scanned in London with (A) TE_{1L} (0.71 ms) and (B) TE_{2L} (1.2 ms). (C) Equivalent plot for ΔR_2^*.
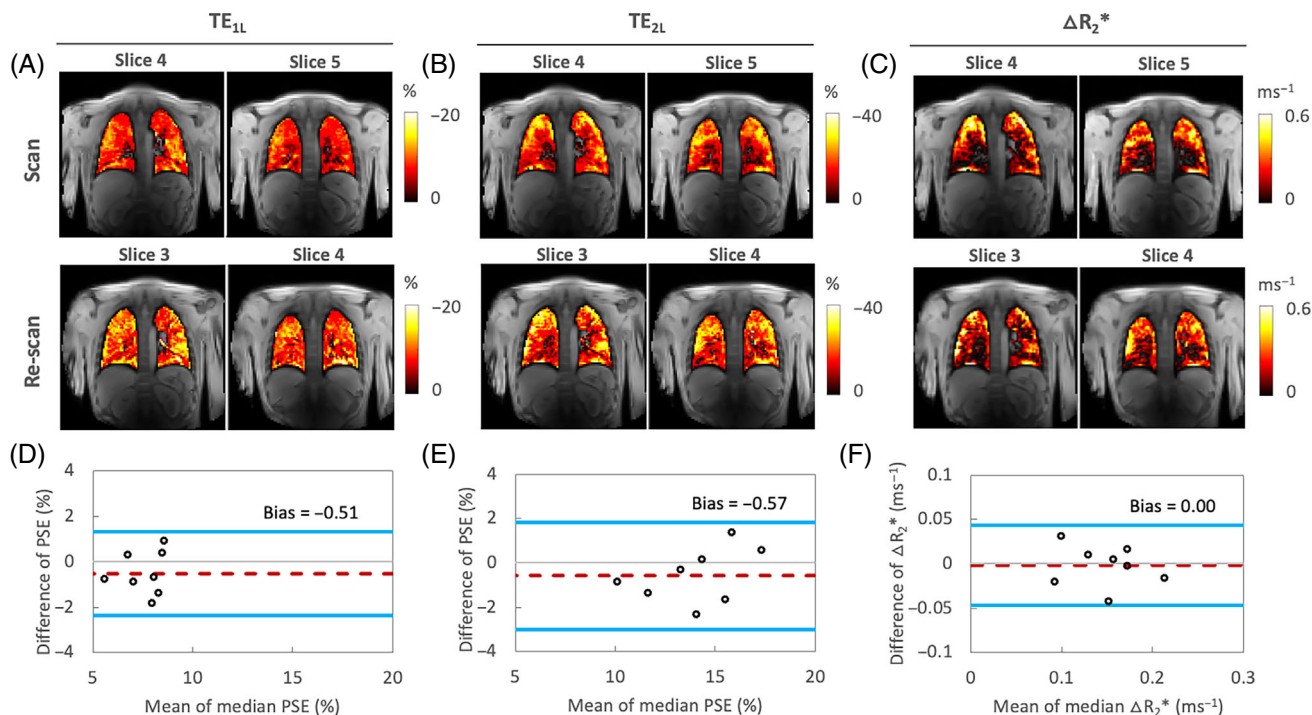
FIGURE 5 Example of one subject and Bland–Altman analysis comparing PSE and $\triangle R_2^*$ between two separate sessions (repeatability) in London. (A) mean PSE with TE = 0.71 ms, (B) mean PSE with TE = 1.2 ms, (C) mean $\triangle R_2^*$, and (D, E) Bland–Altman plots for the repeated measurements of PSE from the first and second TE and (F) $\triangle R_2^*$ (intra-scanner, intra-subject). (A, B) The mean PSE values from eight healthy volunteers varied little between the repeat scans ($-7.39\% \pm 1.61\%$ and $-7.79\% \pm 1.58\%$ at TE_{1L}; $-13.71\% \pm 2.96\%$ and $-14.27\% \pm 2.31\%$ at TE_{2L}). (D–F) The data points correspond to individual participants for difference between two visits to London site.

The $\triangle R_2^*$ maps display a lack of enhancement near major vasculature (Figure 6C). Notably, the $\triangle R_2^*$ maps obtained from the Manchester site continue to show increased noise, a pattern consistent with the TE_{2M} PSE maps. Nevertheless, $\triangle R_2^*$ comparison between two different scanners again shows little evidence of bias, with the 95% LOA measurements being (-0.06%, 0.06%) (Figure 6D). The values of ICC and RDC observed for inter-scanner $\triangle R_2^*$ comparisons reflect good reproducibility (Table 2).

The ICC_{inter} measurement of the log-transformed τ-nBR values shows fair repeatability and reproducibility, while ICC_{intra}, RC, and RDC values are in the poor range due to existence of outliers as shown in Figure S5.

4 | DISCUSSION

In recent years, installations of a clinical 3T MR systems have significantly increased worldwide, often motivated by the higher SNR, relative to lower field systems. However, the viability of dynamic lung OE-MRI at 3T has not to date been investigated. In this work, we demonstrate the feasibility of detecting dynamic OE signal change and quantifying ΔR_2^* due to oxygen breathing at 3T. To

progress the translation of these biomarkers toward clinical use, we also evaluate the intra-scanner repeatability and the inter-scanner/cross-site reproducibility of the proposed method. While a limited number of studies, to date, have demonstrated the feasibility of 3T T_1-weighted OE-MRI,[11–13] our present study is the first report to analyze detailed T_2^*-weighted dynamic signal enhancement behavior, repeatability and reproducibility at 3T. Additionally, this investigation simultaneously entails the quantification of O_2-induced ΔR_2^*.

Our motivation for focussing on T_2^*-related contrast at 3T is twofold. First, the longitudinal relaxivity of O_2 is approximately 20% lower at 3T than 1.5T,[14] leading to a proportionally smaller achievable ΔR_1 at 3T. Secondly, T_2^* in lung decreases with field strength, meaning that SNR in T_1-weighted OE-MRI is much reduced. T_2^*-based OE-MRI has been proposed to counter some of these detrimental effects, although previously-developed methods employed non-standard acquisition methods.[29] Of note, T_2^*-related signal is potentially more specific to ventilation as it is expected to be an effect of changing concentrations of oxygen gas in the alveoli rather than dissolved oxygen.[15] In the present study, we optimized a multi-slice dual-echo RF-spoiled gradient echo acquisition; this method enables measurement of dynamic OE signal change at high

TABLE 3 Repeatability and reproducibility for all metrics.

	Mean ± SD	Difference		95% LOA		RC	RDC	ICC_{intra}	ICC_{inter}	$ICC_{inter\text{-}rater}$
		Intra-scanner	Inter-scanner	Intra-scanner	Inter-scanner					
TE_{1L} PSE[a]	−7.59 ± 1.60	−0.51	-	(−2.36, 1.33)	-	2.61	-	0.77	-	0.99
TE_{2L} PSE[a]	−13.98 ± 2.66	−0.57	-	(−2.99, 1.84)	-	3.42	-	0.92	-	0.99
$\triangle R_2*$[b]	0.14 ± 0.03	0.00	0.00	(−0.05, 0.04)	(−0.06, 0.06)	0.06	0.11	0.94	0.70	0.99
Log-transformed τ-nBR[c]	TE_1 0.75 ± 0.18	-	-	-	-	(−0.66, 1.96)	(−0.69, 2.22)	0.28	0.45	0.99
Log-transformed τ-nBR[c]	TE_2 0.81 ± 0.16	-	-	-	-	(−0.56, 1.27)	(−0.58, 1.40)	0.28	0.54	0.99

Note: First column: mean ± SD of each metric. PSE values were computed from the two repeated sessions in London (16 data sets in total) while $\triangle R_2*$, and wash-in time-normalized for breathing rate (τ-nBR) were computed from traveling volunteers at both sites and the two repeated sessions in London (32 data sets in total). The mean value for each metric was averaged across all six slices except that for $\triangle R_2*$ which was averaged across two posterior slices. Middle columns: mean difference between two sessions, the Bland–Altman 95% LOA for inter- and intra-scanner comparisons, RC for intra-scanner comparisons, and RDC for inter-scanner comparisons. Last three columns: ICC for intra-scanner variation (ICC_{intra}), inter-scanner variation (ICC_{inter}), and inter-rater variation ($ICC_{inter\text{-}rater}$) based on absolute agreement, two-way mixed-effects model. Notably, the $ICC_{inter\text{-}rater}$ values exceeded 0.99 for all metrics. The excellent $ICC_{inter\text{-}rater}$ values were expected, as the only manual step is lung segmentation, and the median voxel value for all reported measurements is largely insensitive to differences in lung outlining.

[a] Unit for PSE and associated RC and RDC: %.

[b] Unit for $\triangle R_2*$ and associated RD and RDC: ms^{-1}.

[c] Unitless for log-transformed τ-nBR and associated RC and RDC.
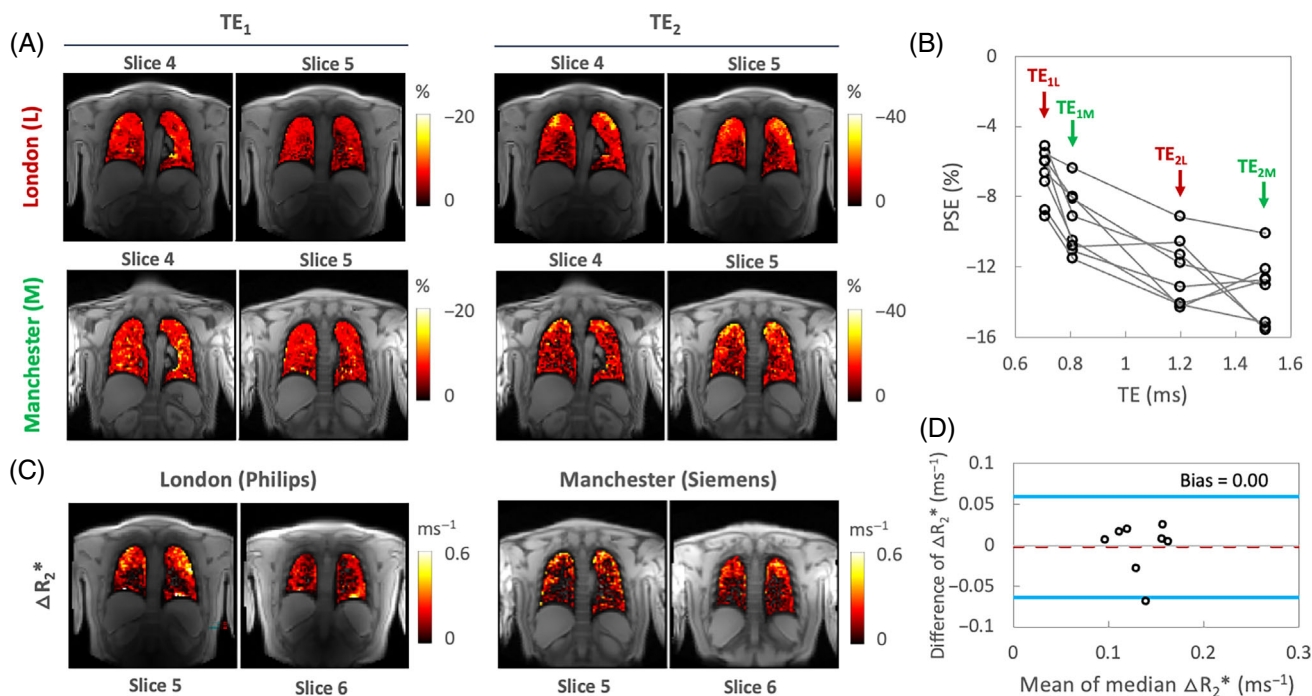
FIGURE 6 (A) An example of inter-scanner intra-subject reproducibility of PSE at TE_1 and TE_2 scanned using two MRI systems at two sites (London and Manchester). (B) PSE obtained at four separate TEs ($TE_{1L} = 0.71$ ms, $TE_{2L} = 1.2$ ms in London and $TE_{1M} = 0.81$ ms, $TE_{2M} = 1.51$ ms in Manchester). The combined PSE values from two MRI systems show a similar trend as a function of TE as the PSE simulation (Figure 1C). (C) Inter-scanner intra-subject reproducibility of $\triangle R_2^*$ from the same subject. (D) Bland–Altman analysis comparing $\triangle R_2^*$ between two scanners for the same subjects.

temporal resolution with controllable T_2^*-weighting, and monitoring of dynamic ΔR_2^*, simultaneously, while requiring no or minimal pulse programming. This easy implementation on standard clinical platforms is intended to assist in clinical translation of this technique.

4.1 | T_2^*-weighting allows good oxygen delivery contrast at 3T

Our simulations (Figure 1D) show the expected dependence of spoiled gradient echo PSE on both ΔT_1 and ΔT_2^*, which can lead to reduced oxygen-related signal change if TE and FA are not optimized. Maximum (negative) PSE for our chosen TR of 16 ms is found with a FA of $\sim5°$ across a wide range of TE (Figure 1A). Our simulations also indicate that negative PSE at TE longer than approximately 0.23 ms when using this FA, is due to the significant oxygen-level dependent ΔR_2^* effect dominating the signal change in the lungs (Figure 1B,D). Our experimental data are consistent with our simulations, with negative PSE observed throughout the lung parenchyma, at levels that are in agreement with simulations. Importantly, this allows the generation of visually high-quality mean PSE maps at the TEs used in this study (Figures 2, 5, 6). The mean PSE values of traveling healthy volunteers (Table 2) are consistent with the expected trend of PSE with

variable TEs from our simulations (Figure 1C). Specifically, the simulated PSE plots, derived from the individual T_2^* values of eight healthy volunteers, demonstrate the significant impact of the chosen T_2^* values on the variability of simulated PSE values (Figure S6). Nonetheless, the experimental PSE values remain within the range of PSE values predicted by simulations.

The mean T_2^* value across all healthy volunteers for 21% O_2 inhalation (0.68 ± 0.05 ms) aligns closely with the literature-reported values (0.74 ± 0.1 ms) at 3T.[30] We observed that upon 100% O_2 inhalation, the mean T_2^* value decreased by about 9% relative to normoxia, resulting in ΔR_2^* of 0.14 ± 0.03 ms^{-1}. To the best of our knowledge, this is the first study that reports mean values of hyperoxic T_2^* and ΔR_2^* of healthy human lungs at 3T. While the influence of T_2^* on PSE is large at 3T, the effect will also be present at lower field strengths when using gradient echo methods and should be accounted for when interpreting nominally T_1-weighted OE-MRI.[17]

4.2 | T_2^*-weighted OE-MRI demonstrates good repeatability and reproducibility

The Bland–Altman, RC, and ICC analysis of the repeated measurements of PSE and $\triangle R_2^*$ suggest high intra-scanner repeatability (Table 3, Figure 5). They also

demonstrate that comparable dynamic OE-MRI protocols for the lung can be implemented at 3T across different sites and scanners with good repeatability and reproducibility for $\triangle R_2$*. While maximum gradient strength and maximum gradient slew rate between the two systems from the different manufacturers are identical, matching TE and bandwidth between scanners proved challenging, which results in variability of OE signal enhancement. For this reason, direct reproducibility assessments for PSE were not feasible although the variation in PSE with TE between scanners closely aligned with our simulations (Figures 1C and 6B). We were able to assess ΔR_2* reproducibility, as T_2* signal decay is, to the best of our knowledge, monoexponential with TE in the lung. In this work, we derived a new metric, τ-nBR, to compensate differences in individual participant's breathing patterns between scans, which have a direct impact on ventilation. The τ-nBR metric showed fair to poor reliability of the dynamic parameter, and this disparity may be attributed to inaccuracies in gas switching time points, impacting on the fitting, as the gas blender was manually operated. Therefore, further investigation is necessary to optimize the enhancement (see Section 4.5 for details).

4.3 | Density correction improves repeatability

While previous studies have demonstrated that density variation due to respiration could provide useful physiological parameters, in the current study, our motivation was to optimize the OE signal. We, therefore, utilized the adapted sponge model, which was introduced by Zha et al.[22] to correct for density variation. In line with the previous reports,[21–24] our results demonstrate that the density correction significantly improves quantification of OE-MRI metrics by decreasing fluctuation due to respiratory motion-induced signal changes (Table 2, Figure S4). This is particularly useful in posterior slices (in supine position) where fluctuation of signal changes is greater (Figure S2).

The accuracy of the sponge model for density correction depends on the assumption that all signal change is due to density variation associated with ventilation. In practice, it is likely that other factors, such as changes in blood volume and local alveolar susceptibility profiles, also influence the signal change during the breathing cycle, and that these factors may vary depending on disease status. Nevertheless, the clear reduction in breathing-related signal variation after correction provides evidence that the density correction is largely successful in our experiments. Furthermore, our results show that the proposed method at 3T yields excellent intra-scanner repeatability

after correction of pixel-wise signal intensity using the deformation fields from image registration (Table 3). Previous studies utilizing a non-Cartesian UTE approach with free-breathing at 1.5T[22] or breath-held acquisitions at 0.55T[10] similarly demonstrated improvement of repeatability in both mean PSE and the low-enhancement percent.

4.4 | Signal variation with position in the lung

Mean signal intensity for both baseline and O_2-induced change is observed to be higher in posterior slices across all subjects due to greater proton density in subject's supine position (Figures 2C,E and S2). Interestingly, we also observed that the absolute PSE of TE_1 gradually decreases, from anterior to posterior slices, across all subjects (Figure 4A) whereas the PSE of TE_2 does not noticeably change (Figure 4B). While PSE combines both ΔT_1 and ΔT_2* effects, the PSE at TE_1 contains a stronger ΔT_1 effect than that at TE_2, as shown in the simulation (Figure 1D). On the contrary, ΔT_2* effect is more substantial and dominating over ΔT_1 effect in the PSE at TE_2. Thus, this may be attributed to increasing effect of ΔT_1 from anterior to posterior, possibly due to increased vessel density and/or blood pooling due to gravity, which require further investigation. A trend of ΔR_2* increase observed from anterior to posterior slices may reflect the expected predominant sensitivity of ΔR_2* to ventilation, as more ventilation is expected in the posterior slices when the lungs are in supine position. This is consistent with a previous report that T_2*-related signal is potentially more specific to ventilation due to an effect of changing concentrations of oxygen gas in the alveoli.[15]

4.5 | Limitations and future directions

The present study has several limitations. First, we employed a 2D multi-slice readout, which was designed to prioritize relatively high temporal resolution and allow reasonable lung coverage while accommodating free-breathing for participant comfort. Although the temporal resolution of 1.54 s is currently the highest achievable resolution in dynamic lung OE-MRI, it cannot still resolve all cardiac and respiratory motion-related artifacts during acquisition. Moreover, a 2D interleaved multi-slice excitation affects the signal variation due to through-slice respiratory motion and inflow of blood, which are likely to be a source of noise for our T_2*-sensitized signal. Additionally, slice gaps and the limited number of slices may mean that some localized pathology could be missed. This

could be mitigated by increasing the number of slices, either by increasing TR (thereby lowering temporal resolution and leading to more motion-related image blurring and artifacts) or by employing acceleration methods. Since there may be inconsistencies between the slice positions, a multi-slice acquisition also leads to challenges for inter-scanner, inter-session image registration that is essential for voxel-wise comparison. The 3D non-Cartesian UTE OE-MRI methods have been demonstrated at 1.5T and lower field strengths to allow isotropic spatial resolution whole lung OE-MRI measurements.[10,17,22,31] However, those studies are limited to static acquisitions which employed either breath-hold or two separate free-breathing sessions of normoxia and hyperoxia. Dynamic OE-MRI using such methods may be possible by employing temporal view sharing methods, but we are unaware of any studies to date that have made use of this strategy. Although currently existing dynamic methods utilize respiratory gating approaches resulting in longer temporal resolution compared to our proposed method, it's worth noting that these 3D dynamic methods offer enhanced spatial resolution and SNR. Consequently, there is a need for future investigations to explore the implementation of 3D UTE acquisition in our proposed method, while maintaining a reasonable temporal resolution.

Second, our study design lacked a reference standard due to the absence of established dynamic OE-MRI methods at 3T. This also aligns with a key motivation of the present study, which focuses on developing a reliable protocol tailored for 3T. Future investigations could compare our methods with OE-MRI at lower field strengths or with other functional lung MRI methods.

Thirdly, low SNR in the current study leads to poor performance in extracting dynamic parameters, particularly wash-in time. Although our results show that PSE and $\triangle R_2^*$ measures are repeatable, these largely reflect steady-state conditions. Nonetheless, our primary aim was to explore a complete free-breathing acquisition approach that spans the entire gas delivery time course for both air and O_2 phase. This approach not only enhances subject comfort but also maintains physiological realism, features that breath-hold or separate free-breathing methods for each gas phase may lack. Therefore, the feasibility of the proposed method with the full free-breathing acquisition suggests potential for future development of OE-MRI for evaluating dynamic parameters. Furthermore, optimizing the methodological approach, such as new hardware for the administration or additional monitoring to track breathing patterns, might improve reproducibility in this measurement.

Lastly, being a proof-of-concept investigation, our current study is limited by a small sample size and the absence of individuals with disease. Future studies will provide a more comprehensive understanding of the method's applicability in such settings.

5 | CONCLUSIONS

Our study establishes the viability of dynamic lung OE-MRI at 3T, optimizing a dual-echo RF-spoiled gradient echo acquisition for simultaneous PSE, R_2^* changes, and oxygen wash-in measurement during free-breathing, offering functional information. Excellent intra-scanner repeatability and good inter-scanner reproducibility of the metrics suggest multi-center clinical application will be feasible. Future studies in respiratory diseases may allow us to better understand the method's potential.

CONFLICT OF INTEREST STATEMENT
G.J.M. Parker is an employee of and holds ownership interest (including patents) in Bioxydyn Limited. J. Naish and M. Tibiletti are employees of Bioxydyn Limited. No potential conflicts of interest were disclosed by the other authors.

ORCID
Mina Kim https://orcid.org/0000-0001-9779-4414
Josephine H. Naish https://orcid.org/0000-0002-8980-8924
Sarah H. Needleman https://orcid.org/0000-0001-6137-9075
Yohn Taylor https://orcid.org/0000-0002-0407-6454
Geoff J. M. Parker https://orcid.org/0000-0003-2934-2234

REFERENCES
1. Edelman RR, Hatabu H, Tadamura E, Li W, Prasad PV. Non-invasive assessment of regional ventilation in the human lung using oxygen-enhanced magnetic resonance imaging. *Nat Med.* 1996;2:1236-1239.

2. Ohno Y, Hatabu H, Takenaka D, Van Cauteren M, Fujii M, Sugimura K. Dynamic oxygen-enhanced MRI reflects diffusing capacity of the lung. *Magn Reson Med*. 2002;47:1139-1144.

3. Jakob PM, Wang T, Schultz G, Hebestreit H, Hebestreit A, Hahn D. Assessment of human pulmonary function using oxygen-enhanced T(1) imaging in patients with cystic fibrosis. *Magn Reson Med*. 2004;51:1009-1016.

4. Renne J, Lauermann P, Hinrichs JB, et al. Chronic lung allograft dysfunction: oxygen-enhanced T1-mapping MR imaging of the lung. *Radiology*. 2015;276:266-273.

5. Ohno Y, Hatabu H, Takenaka D, Adachi S, Van Cauteren M, Sugimura K. Oxygen-enhanced MR ventilation imaging of the lung: preliminary clinical experience in 25 subjects. *AJR Am J Roentgenol*. 2001;177:185-194.

6. Molinari F, Eichinger M, Risse F, et al. Navigator-triggered oxygen-enhanced MRI with simultaneous cardiac and respiratory synchronization for the assessment of interstitial lung disease. *J Magn Reson Imaging*. 2007;26:1523-1529.

7. Ohno Y, Iwasawa T, Seo JB, et al. Oxygen-enhanced magnetic resonance imaging versus computed tomography: multicenter study for clinical stage classification of smoking-related chronic obstructive pulmonary disease. *Am J Respir Crit Care Med*. 2008;177:1095-1102.

8. Salem A, Little RA, Latif A, et al. Oxygen-enhanced MRI is feasible, repeatable, and detects radiotherapy-induced change in hypoxia in xenograft models and in patients with non-small cell lung cancer. *Clin Cancer Res*. 2019;25:3818-3829.

9. Stadler A, Stiebellehner L, Jakob PM, et al. Quantitative and O2 enhanced MRI of the pathologic lung: findings in emphysema, fibrosis, and cystic fibrosis. *Int J Biomed Imaging*. 2007;2007:23624-23627.

10. Bhattacharya I, Ramasawmy R, Javed A, et al. Oxygen-enhanced functional lung imaging using a contemporary 0.55 T MRI system. *NMR Biomed*. 2021;34:e4562.

11. Thieme SF, Dietrich O, Maxien D, et al. Oxygen-enhanced MRI of the lungs: intraindividual comparison between 1.5 and 3 tesla. *Rofo*. 2011;183:358-364.

12. Halaweish AF, Charles HC. Physiorack: an integrated MRI safe/conditional, gas delivery, respiratory gating, and subject monitoring solution for structural and functional assessments of pulmonary function. *J Magn Reson Imaging*. 2014;39:735-741.

13. Ohno Y, Yui M, Yoshikawa T, et al. 3D oxygen-enhanced MRI at 3T MR system: comparison with thin-section CT of quantitative capability for pulmonary functional loss assessment and clinical stage classification of COPD in smokers. *J Magn Reson Imaging*. 2021;53:1042-1051.

14. Bluemke E, Stride E, Bulte DP. A simplified empirical model to estimate oxygen relaxivity at different magnetic fields. *NMR Biomed*. 2022;35:e4625.

15. Pracht ED, Arnold JF, Wang T, Jakob PM. Oxygen-enhanced proton imaging of the human lung using T2. *Magn Reson Med*. 2005;53:1193-1196.

16. O'Connor JP, Aboagye EO, Adams JE, et al. Imaging biomarker roadmap for cancer studies. *Nat Rev Clin Oncol*. 2017;14:169-186.

17. Kruger SJ, Fain SB, Johnson KM, Cadman RV, Nagle SK. Oxygen-enhanced 3D radial ultrashort echo time magnetic resonance imaging in the healthy human lung. *NMR Biomed*. 2014;27:1535-1541.

18. Dietrich O, Raya JG, Fasol U, Peller M, Reiser MF, Schoenberg SO. Oxygen-enhanced MRI of the lung at 3 tesla: feasibility and T1 relaxation times. *Proc Intl Soc Magn Reson Med*. 2006;14:1307.

19. Avants BB, Epstein CL, Grossman M, Gee JC. Symmetric diffeomorphic image registration with cross-correlation: evaluating automated labeling of elderly and neurodegenerative brain. *Med Image Anal*. 2008;12:26-41.

20. Avants BB, Tustison NJ, Song G, Cook PA, Klein A, Gee JC. A reproducible evaluation of ANTs similarity metric performance in brain image registration. *Neuroimage*. 2011;54:2033-2044.

21. Pusterla O, Bauman G, Wielputz MO, et al. Rapid 3D in vivo 1H human lung respiratory imaging at 1.5 T using ultra-fast balanced steady-state free precession. *Magn Reson Med*. 2017;78:1059-1069.

22. Zha W, Kruger SJ, Johnson KM, et al. Pulmonary ventilation imaging in asthma and cystic fibrosis using oxygen-enhanced 3D radial ultrashort echo time MRI. *J Magn Reson Imaging*. 2018;47:1287-1297.

23. Staring M, Bakker ME, Stolk J, Shamonin DP, Reiber JH, Stoel BC. Towards local progression estimation of pulmonary emphysema using CT. *Med Phys*. 2014;41:021905.

24. Zha W, Cadman RV, Hahn AD, Johnson KM, Fain SB. Dynamic 3D isotropic resolution imaging of human lungs using oxygen-enhanced radial UTE MRI. *Proc Intl Soc Magn Reson Med*. 2018:1086.

25. Raunig DL, McShane LM, Pennello G, et al. Quantitative imaging biomarkers: a review of statistical methods for technical performance assessment. *Stat Methods Med Res*. 2015;24:27-67.

26. Obuchowski NA. Interpreting change in quantitative imaging biomarkers. *Acad Radiol*. 2018;25:372-379.

27. Pleil JD, Wallace MAG, Stiegel MA, Funk WE. Human biomarker interpretation: the importance of intra-class correlation coefficients (ICC) and their calculations based on mixed models, ANOVA, and variance estimates. *J Toxicol Environ Health B Crit Rev*. 2018;21:161-180.

28. Shrout PE, Fleiss JL. Intraclass correlations: uses in assessing rater reliability. *Psychol Bull*. 1979;86:420-428.

29. Triphan SM, Breuer FA, Gensler D, Kauczor HU, Jakob PM. Oxygen enhanced lung MRI by simultaneous measurement of T1 and T2* during free breathing using ultrashort TE. *J Magn Reson Imaging*. 2015;41:1708-1714.

30. Yu J, Xue Y, Song HK. Comparison of lung T2* during free-breathing at 1.5 T and 3.0 T with ultrashort echo time imaging. *Magn Reson Med*. 2011;66:248-254.

31. Xu P, Zhang J, Nan Z, Meersmann T, Wang C. Free-breathing phase-resolved oxygen-enhanced pulmonary MRI based on 3D stack-of-stars UTE sequence. *Sensors (Basel)*. 2022;22:3270.

SUPPORTING INFORMATION

Additional supporting information may be found in the online version of the article at the publisher's website.

Table S1. Simulation parameters.

Table S2. Shapiro–Wilk normality test before and after log-transformation of τ-nBR values. The *p*-values below 0.05 suggests that the data significantly deviates from a normal distribution.

Figure S1. A workflow diagram summarizing the experimental study population and data analysis.

Figure S2. Example time course curves of the median signal intensity (SI) and R_2^* from masked, registered lung for each slice of a single traveling subject obtained in London (A) and Manchester (B) with TE_{1L} (0.71 ms), TE_{2L} (1.2 ms), TE_{1M} (0.81 ms), and TE_{2M} (1.51 ms), by pre- (blue line) and post-tissue density correction (red line).

Figure S3. (A) Pre- and (B) post-density corrected example time course (blue dashed lines) and fits (red solid lines) for downslopes and upslopes from an individual voxel.

Figure S4. The Bland–Altman plots for the repeated measurements of percent signal change (PSE) averaged over two posterior slices from the 1st and 2nd TE before (A, C for TE_{1L} and TE_{2L}, respectively) and after tissue density correction (B, D for TE_{1L} and TE_{2L}, respectively). The 95% LOA decreased from (−7.22%, 4.55%) to (−2.36%, 1.33%) for TE_{1L} and (−7.53%, 6.20%) to (−2.99%, 1.84%) for TE_{2L}. Similarly, additional statistical metrics display significantly reduced RC (69% and 65% for TE_{1L} and TE_{2L}, respectively) and increased ICC_{intra} (94% and 75% for TE_{1L} and TE_{2L}, respectively) with tissue density correction compared to pre-density correction.

Figure S5. Bland–Altman analysis plots illustrating the repeated measurements of wash-in time normalized for breathing rate (non-transformed breathing rate [τ-nBR]; unitless) representing the breath count during τ, for the 1st and 2nd TE. The data points correspond to individual participants for inter-scanner difference between two visits to Manchester and London sites (A, B) and intra-scanner difference between two scans in London site (C, D). See also Table 3.

Figure S6. Simulated versus experimental percent signal change (PSE) values plotted as a function of TE. For the simulation, we utilized literature-reported values for T_1 (1281 ms for air and 1102 ms for 100% O_2) and incorporated measured T_2^* values from the lungs at air and 100% O_2 breathing, acquired using the same experimental protocol as detailed in this study (Table S1). For each traveling volunteer, we averaged T_2^* values across two sites (London and Manchester) from two posterior slices. These averaged T_2^* values for eight volunteers listed on the right-hand side (as displayed in Table S1 of the supporting information) were used to simulate eight individual PSE plots. The experimental PSE values were obtained at four separate echo times ($TE_{1L} = 0.71$ ms, $TE_{2L} = 1.2$ ms in London and $TE_{1M} = 0.81$ ms, $TE_{2M} = 1.51$ ms in Manchester) and averaged across multiple either (A) two posterior or (B) all six slices for each traveling volunteer. The collective PSE results from the two MRI systems exhibit a comparable trend in relation to the TE while the simulated PSE plots show variability influenced by individual T_2^* values.